IEICE TRANS. COMMUN., VOL.E107–B, NO.8 AUGUST 2024

PAPER

Differential Active Self-Interference Cancellation for Asynchronous In-Band Full-Duplex GFSK

Shinsuke IBI [†a)], ***Senior Member***, **Takumi TAKAHASHI** [††], ***Member***, ***and*** **Hisato IWAI**[†], ***Fellow***

SUMMARY This paper proposes a novel differential active self-interference canceller (DASIC) algorithm for asynchronous in-band full-duplex (IBFD) Gaussian filtered frequency shift keying (GFSK), which is designed for wireless Internet of Things (IoT). In IBFD communications, where two terminals simultaneously transmit and receive signals in the same frequency band, there is an extremely strong self-interference (SI). The SI can be mitigated by an active SI canceller (ASIC), which subtracts an interference replica based on channel state information (CSI) from the received signal. The challenging problem is the realization of asynchronous IBFD for wireless IoT in indoor environments. In the asynchronous mode, pilot contamination is induced by the non-orthogonality between asynchronous pilot sequences. In addition, the transceiver suffers from analog front-end (AFE) impairments, such as phase noise. Due to these impairments, the SI cannot be canceled entirely at the receiver, resulting in residual interference. To address the above issue, the DASIC incorporates the principle of the differential codec, which enables to suppress SI without the CSI estimation of SI owing to the differential structure. Also, on the premise of using an error correction technique, iterative detection and decoding (IDD) is applied to improve the detection capability while exchanging the extrinsic log-likelihood ratio (LLR) between the maximum *a-posteriori* probability (MAP) detector and the channel decoder. Finally, the validity of using the DASIC algorithm is evaluated by computer simulations in terms of the packet error rate (PER). The results clearly demonstrate the possibility of realizing asynchronous IBFD.

key words: *asynchronous in-band full-duplex, pilot contamination, GFSK, active self-interference canceller, differential encoder, iterative detection and decoding, analog front-end impairment*

1. Introduction

Wireless Internet of Things (IoT) is now spreading rapidly due to the demand for big databases for machine learning-aided decision-making and control in sensor networks. Classical Bluetooth, as well as Bluetooth low energy (BLE), have been widely installed in commercial products that require power-saving functionality, such as sensors, remote control units, personal computer (PC) peripherals, smartwatches, and so on [1], [2]. The Bluetooth family utilizes Gaussian frequency-shift keying (GFSK) [3], [4], which achieves high power efficiency without nonlinear distortion in the power amplifier (PA) at the transmitter. Although GFSK is a classical modulation technique, it might be vital in constructing IoT information infrastructure. This paper focuses mainly on in-band full-duplex (IBFD) mutual communications for wireless IoT.

IBFD is a technique in which two nodes (terminals) simultaneously transmit and receive signals in the same frequency band. In recent years, the study of IBFD has attracted much attention from both theoretical and practical standpoints [5]–[7]. Even in spectrum utilization for 5G mobile communication systems, a reasonable implementation method is one of the topics of current interest [8]–[10]. Compared with half-duplex (HD), such as time division duplex (TDD) and frequency division duplex (FDD), the advantage of IBFD is that a 50% reduction in wireless resource occupancy can be achieved.

When nodes A and B cooperatively perform IBFD communication, node A transmits its own signal to node B and simultaneously receives the signal transmitted from node B. In addition to the signal arriving from node B, the signal of node A itself is included in the received signal at node A as self-interference (SI). SI is usually mitigated by a combination of passive and active interference cancellers [11]–[13]. In the passive canceller, an antenna structure is designed to enhance the path loss of the SI signals [13]. On the other hand, in the active canceller, SI is eliminated as much as possible by subtracting a replica of SI from the received signal. Ideally, the replica is regenerated because its own signal is perfectly known at the receiver of node A [11], [14]. Thus, in a broad sense, IBFD is a type of physical layer network-coded communication [15], [16].

However, the receiver of IBFD suffers from severe residual SI even after the passive interference cancellation, resulting in a low signal-to-interference power ratio (SIR). An analog-to-digital converter (ADC) is an essential interface with analog baseband signals for sophisticated digital signal processing in the physical layer. A lower SIR requires a higher resolution of ADC to avoid the disappearance of the desired signal component or fatal information loss, and it is not undesirable in terms of hardware implementation [17]–[19]. To alleviate the inconvenience caused by the low SIR, it is necessary to actively cancel SI in the analog domain at the front stage of the ADC [11], [20]. Typically, the active SI cancellation capability relies on the accuracy of the self-channel state information (CSI) of SI. In other words, the channel estimation should be conducted with the aid of a pilot sequence before invoking IBFD transmissions. Therefore, the synchronous frame format of the signals and medium access control (MAC) should be appropriately designed [21], [22]. Furthermore, in [12], [23], it is shown

Manuscript received July 10, 2023.
Manuscript revised November 11, 2023.
Manuscript publicized February 16, 2024.

[†]Faculty of Science and Engineering, Doshisha University, Kyotanabe-shi, 610-0394 Japan.
[††]Graduate School of Engineering, Osaka University, Suita-shi, 565-0871 Japan.
a) E-mail: sibi@mail.doshisha.ac.jp

DOI: 10.23919/transcom.2023EBP3119

Copyright © 2024 The Institute of Electronics, Information and Communication Engineers

that analog front-end (AFE) impairments, such as the IQ imbalance of the IQ mixers, nonlinear distortion of the PA, and phase noise at the local oscillators (LOs), are crucial problems for the active canceller. As a result, it is subject to residual SI in the analog domain, and the residuals are suppressed by the additional active canceller in the digital domain after the ADC.

In many wireless IoT scenarios, the communication link establishment is event-driven. Nodes A and B are not always in a full-buffer state, i.e., there is a possibility not to have a data message to send, resulting in the HD mode. Nevertheless, to invoke the IBFD mode anytime, the CSI should be periodically updated at the expense of pilot overhead signals. Due to the increased overheads, IBFD is not suitable for event-driven communications. Because the amount of data is considered small, the data should be sent in HD mode instead of frequent transmission of pilot signals. Alternatively, it is also possible to estimate the CSI for every IBFD request. However, orthogonal pilot sequences should be synchronously sent from both nodes A and B. If the strength of the node B signal is low, the pilot contamination is small, even in the case of non-orthogonal pilot usage. In this paper, the target SIR ranges between -20 and -10 [dB] in indoor environments. It means relatively high strength of the node B signal, resulting in severe pilot contamination. To solve this problem, it is practical to use pilot overheads that are orthogonal to each other at nodes A and B.

In the event-driven scenario, asynchronous IBFD is preferable. Due to the asynchronous mode, it is impossible to guarantee the orthogonality of pilot sequences, resulting in "pilot contamination," which induces residual SI after the active canceller. Asynchronous IBFD has been studied in a few papers so far [24]–[27]. However, most ideas rely on interference avoidance networking in MAC protocol aspects. Therefore, these papers motivate us to consider how to realize *the effective asynchronous SI canceller in pilot contamination environments* from the viewpoint of physical layer aspects.

Motivated by the above, this paper presents a differential active SI canceller (DASIC) that incorporates the principle of the differential codec. Without AFE impairments, the DASIC is capable of eliminating SI without self-CSI estimation. As a result, the communication links are asynchronously established, making them suitable for event-driven communications. However, the DASIC yields superposed signals of plural transmitted symbols, resulting in low reception sensitivity. This issue is relaxed by maximum *a-posteriori* probability (MAP) detection [28], [29]. Under the differential structure, on the premise of using an error correction code (ECC) technique of channel coding, iterative signal detection and decoding (IDD), which improves signal detection capability while exchanging the extrinsic log-likelihood ratio (LLR) between the MAP detector and the channel decoder [30]–[33], is also designed.

As a notable approach to reduce the computational complexity involved in the detection process, neural network (NN)-aided detectors attract attention for detecting signals or channel states under unknown statistical model behavior [34], [35]. In principle, wireless environments in the training phase of network structure should be the same as the test phase. Otherwise, the mismatch of the structure deteriorates detection capability. To overcome the penalty, the deep-unfolding technique [36], [37] is useful to improve the robustness against the model error. The proposed DASIC algorithm fully captures the statistical behavior by MAP algorithm with a few states. Therefore, there are no model mismatch errors, and the NN technique is structurally unnecessary.

The contributions of this paper are summarized as follows:

1. A DASIC for blind SI cancellation without self-CSI estimations, which enables asynchronous IBFD, is proposed.
2. To improve the detection capability, IDD for the DASIC is investigated from the standpoint of the packet error rate (PER) performance.
3. The negative effects of the AFE impairments are evaluated by computer simulations.

To the best of the authors' knowledge, this is the first paper that proposes asynchronous IBFD with the aid of differential signal structure for blind SI cancellation in terms of physical layer aspects.

The rest of this paper is organized as follows. Section 2 presents a schematic of the IBFD transceiver for GFSK signaling in the context of the signal model. In Sect. 3, the DASIC algorithm for blind SI cancellation is proposed. Section 4 describes signal detection algorithms designed on the basis of observations of the DASIC output from standpoints of computational complexity and detection capability. The proposed method with and without AFE impairments is validated by computer simulations in Sect. 5. Finally, Sect. 6 concludes the paper with a summary.

The mathematical notation employed in this paper is as follows. The continuous time and discrete time indexes are denoted by (t) and $[k]$, respectively. $\mathbb{R}$ and $\mathbb{C}$ represent the fields of real numbers and complex numbers, respectively. $\mathfrak{R}\{\cdot\}$ indicates the real part of complex numbers. The imaginary unit $\sqrt{-1}$ is denoted by j. $\Pr[a|b]$ and $p(a|b)$, respectively, represent the conditional probability mass function (PMF) and the probability density function (PDF) of an event a given the occurrence of an event b. $\mathbb{E}\{\cdot\}$ indicates an expected value.

2. Signal Model

This section formulates a signal model for the IBFD GFSK transceiver illustrated in Fig. 1. Nodes A and B simultaneously transmit and receive signals in the same frequency channel to communicate with each other. The transmitted RF signal $s_i(t) \in \mathbb{R}$ of each A and B is expressed as

$$s_i(t) = \sqrt{2}\alpha \mathfrak{R}\left\{x_i(t)\xi_i(t)\right\}, \tag{1}$$

$$\xi_i(t) = \exp\left[\mathrm{j}(\omega_i t + \theta_i(t))\right], \tag{2}$$

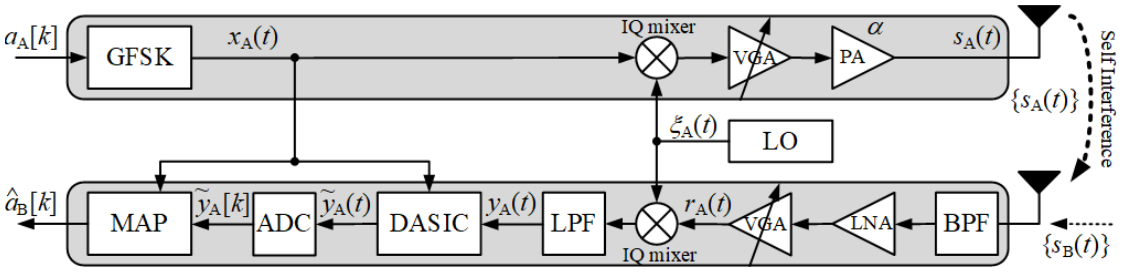

Fig. 1 Block diagram of IBFD GFSK transceiver.

where $i \in \{\mathrm{A},\mathrm{B}\}$. α is the amplitude of transmitted RF signal, and $\omega_i = \omega_\mathrm{c} + \omega_i^\mathrm{o}$ is angle frequency with offset ω_i^o, where ω_c is the center angle of frequency. More specifically, $\omega_\mathrm{A} = \omega_\mathrm{c} + \omega_\mathrm{A}^\mathrm{o}$ and $\omega_\mathrm{B} = \omega_\mathrm{c} + \omega_\mathrm{B}^\mathrm{o}$. It is noteworthy that ω_A is not equal to ω_B. Furthermore, $\theta_i(t) = \theta_i'(t) + \theta_i^\mathrm{o}$ is the phase noise with offset θ_i^o, where $\theta_i'(t)$ obeys random-walk. The complex-valued baseband (CBB) signal $x_i(t) \in \mathbb{C}$ is represented by

$$x_i(t) = \exp\left[\mathrm{j}\phi_i(t)\right], \tag{3}$$

where $\phi_i(t)$ is an information-bearing variable. Denoting the energy and time duration of one symbol by E_s and T_s, respectively, the amplitude is expressed as $\alpha = \sqrt{E_\mathrm{s}/T_\mathrm{s}}$. The amplitude is controlled by the variable gain amplifier (VGA) and PA with ideal characteristics.

Supposing that nodes A and B obey the same modulation rule, the information-bearing variable $\phi_i(t)$ during the interval $kT_\mathrm{s} \le t(= t' + kT_\mathrm{s}) < (k+1)T_\mathrm{s}$ is represented as

$$\phi_i(t) = 2\pi\eta \sum_{l=k-L+1}^{k} a_i[l]q(t' + (k-l)T_\mathrm{s}) + \pi\eta \sum_{l'=0}^{k-L} a_i[l'], \tag{4}$$

where $a_i[k] \in \{-1, 1\}$ is a message bit in a bipolar expression, η is a modulation index, and L is the memory size that is determined by $B_\mathrm{G}T_\mathrm{s}$. Here, B_G is the 3–dB sideband of the Gaussian filter. In this paper, minimum shift keying (MSK) with ($\eta = 0.5, B_\mathrm{G}T_\mathrm{s} = \infty$) and Gaussian filtered MSK (GMSK) with ($\eta = 0.5, B_\mathrm{G}T_\mathrm{s} = 0.5$) are used.

The function $q(t)$ represents a phase pulse, which is defined by [38]

$$q(t) = \int_{-\infty}^{t} g(\tau)d\tau, \tag{5}$$

under a constraint of

$$q(t) = \begin{cases} 0 & t \le 0 \\ 1/2 & t > LT_\mathrm{s} \end{cases}. \tag{6}$$

The function $g(\tau)$ is a frequency pulse given by

$$g(\tau) = \frac{1}{2T_\mathrm{s}}\left[Q\left(2\pi B_\mathrm{G}\frac{\tau - \frac{T_\mathrm{s}}{2}}{\sqrt{\ln 2}}\right) - Q\left(2\pi B_\mathrm{G}\frac{\tau + \frac{T_\mathrm{s}}{2}}{\sqrt{\ln 2}}\right)\right], \tag{7}$$

where $Q(\cdot)$ is the Q function.

In this paper, let us focus on the signal detection of node B's message at node A[†]. The received RF signal $r_\mathrm{A}(t)$ after the band-pass filter (BPF) is given by

$$\begin{aligned} r_\mathrm{A}(t) = \; & \Re\left\{h_\mathrm{AA}\sqrt{2}\alpha x_\mathrm{A}(t+\tau_\mathrm{A})\xi_\mathrm{A}(t+\tau_\mathrm{A})\right\} \\ & + \Re\left\{h_\mathrm{AB}\sqrt{2}\alpha x_\mathrm{B}(t+\tau_\mathrm{B})\xi_\mathrm{B}(t+\tau_\mathrm{B})\right\} + n_\mathrm{A}(t), \end{aligned} \tag{8}$$

where $h_\mathrm{AA} \in \mathbb{C}$ and $h_\mathrm{AB} \in \mathbb{C}$ are the complex-valued channel coefficients of the A − A and A − B links, respectively, which reflect the impacts of path loss, shadowing, and fading phenomena. h_AA and h_AB obey flat Rayleigh fading without frequency selectivity. The propagation delay time is denoted by τ_i. Furthermore, $n_\mathrm{A}(t) \in \mathbb{R}$ is a noise term.

The CBB signal $y_\mathrm{A}(t)$ after low-noise amplifier (LNA), VGA, IQ mixer, and ideal low-pass filter (LPF) processes is expressed as

$$\begin{aligned} y_\mathrm{A}(t) &= \sqrt{2}\left\{r_\mathrm{A}(t)\xi_\mathrm{A}^*(t)\right\}_\mathrm{LPF} \\ &= h_\mathrm{AA}\kappa_\mathrm{AA}(t)\alpha x_\mathrm{A}(t+\tau_\mathrm{A}) \\ &\quad + h_\mathrm{AB}\kappa_\mathrm{AB}(t)\alpha x_\mathrm{B}(t+\tau_\mathrm{B}) + z_\mathrm{A}(t), \end{aligned} \tag{9}$$

where the noise term is $z_\mathrm{A}(t) = \sqrt{2}\left\{n_\mathrm{A}(t)\xi_\mathrm{A}^*(t)\right\}_\mathrm{LPF}$, which is modeled by complex-valued Gaussian noise with zero mean and $\beta \triangleq N_0/T_\mathrm{s}$ variance. Note that N_0 is the noise energy for one symbol's time duration, whereas β is the noise density. $\kappa_{\mathrm{A}i}(t)$, ($i \in \{\mathrm{A},\mathrm{B}\}$), represents LO impairments of both nodes, which is given by

$$\kappa_{\mathrm{A}i}(t) = \xi_i(t+\tau_i)\xi_\mathrm{A}^*(t) = \kappa_{\mathrm{A}i}'(t)\kappa_{\mathrm{A}i}^\mathrm{o}, \tag{10}$$

$$\kappa_{\mathrm{A}i}'(t) = \exp\left[\mathrm{j}(\theta_i'(t+\tau_i) - \theta_\mathrm{A}'(t))\right], \tag{11}$$

$$\kappa_\mathrm{AA}^\mathrm{o} = 1, \tag{12}$$

$$\kappa_\mathrm{AB}^\mathrm{o} = \exp\left[\mathrm{j}(\omega_\mathrm{B}^\mathrm{o} - \omega_\mathrm{A}^\mathrm{o})\right]\exp\left[\mathrm{j}(\theta_\mathrm{B}^\mathrm{o} - \theta_\mathrm{A}^\mathrm{o})\right]. \tag{13}$$

In IBFD systems, the longer distance between nodes A and B induces a stronger SI because $|h_\mathrm{AA}|^2$ is much higher than $|h_\mathrm{AB}|^2$. Now, let us denote the SIR by

$$\zeta = \frac{|h_\mathrm{AB}|^2}{|h_\mathrm{AA}|^2}. \tag{14}$$

In principle, the signal components of $h_\mathrm{AB}x_\mathrm{B}(t)$ disappear or deteriorate after the ADC while it is subject to the huge difference between $|h_\mathrm{AA}|^2$ and $|h_\mathrm{AB}|^2$, i.e., extremely low ζ. Thus, the SI of the first term of the right-hand side in

[†]The signal detection of node A's message at node B is readily explained by replacing the variables.

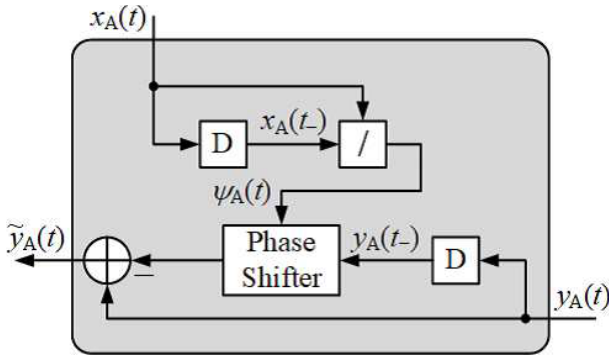

Fig. 2 Block diagram of the DASIC process.

Eq. (8) should be canceled before the ADC process, i.e., in the analog domain. Assuming that $h'_{AA} \triangleq h_{AA}\alpha\xi_A(t+\tau_A)$ is accurately estimated at the receiver, a typical active SI canceller (ASIC) ideally subtracts the replica of the SI from the received signal as

$$r_A(t) - \Re\left\{h'_{AA}x_A(t+\tau_A)\right\}. \tag{15}$$

Instead of using an ASIC, this study employs a DASIC for blindly canceling the SI in a regime of differential detection without knowledge of $h_{AA}\alpha\xi_A(t+\tau_A)$. The CBB signal $\tilde{y}_A(t)$ is extracted from the output of the DASIC. Finally, the MAP detector yields the estimates $\hat{a}_B[k]$ of node B's message.

3. Principle of DASIC

A schematic of the DASIC is illustrated in Fig. 2, which is intended as an analog circuit. It is assumed that an analog multiplier is used for division and a mixer is used for phase adjustment; hence, a significant increase in power consumption is not expected owing to the use of passive elements. The problem arising here is the realization of a delay of one symbol duration of an analog signal. This paper assumes that this delay can be achieved ideally. There are still many issues to be solved in the implementation of analog circuits, which we regard as a future issue[†].

More specifically, by observing the CBB signal $x_A(t)$, a phase shift is generated as

$$\psi_A(t) = \frac{x_A(t)}{x_A(t-T_s)}. \tag{16}$$

Then, assuming an ideal delay circuit, the phase of a delayed CBB signal $y_A(t-T_s)$ is shifted by $\psi_A(t)$ at the phase shifter. Denoting $t_- = t - T_s$ to simplify the mathematical notations, we have the modified differential signal, which is represented as

$$\begin{aligned} y_A(t_-)\psi_A(t) &= h_{AA}\alpha x_A(t) + \varepsilon_A(t) \\ &\quad + h_{AB}\kappa_{AB}(t)\alpha x_B(t_- + \tau_B)\psi_A(t) \\ &\quad + z_A(t_-)\psi_A(t), \end{aligned} \tag{17}$$

where

$$\varepsilon_A(t) = h_{AA}\alpha\left[\kappa_{AA}(t)x_A(t+\tau_A) - x_A(t)\right]. \tag{18}$$

Equations (10)–(12) indicate that $\varepsilon_A(t)$ is zero if the propagation delay τ_A of SI is zero. In other words, the additional noise component $\varepsilon_A(t)$ is induced by the propagation delay time τ_A.

Eventually, the analog interference canceller is operated as

$$\begin{aligned} \tilde{y}_A(t) &= y_A(t) - y_A(t_-)\psi_A(t) \\ &= \tilde{h}_{AB}\alpha\tilde{x}_B(t+\tau_B) + \tilde{\varepsilon}_A(t) + \tilde{z}_A(t), \end{aligned} \tag{19}$$

where we have

$$\tilde{h}_{AB} = h_{AB}\kappa^{o}_{AB}, \tag{20}$$

$$\tilde{x}_B(t+\tau_B) = x_B(t+\tau_B) - \psi_A(t)x_B(t_- + \tau_B), \tag{21}$$

$$\begin{aligned} \tilde{\varepsilon}_A(t) &= \varepsilon_A(t) + \tilde{h}_{AB}[\kappa'_{AB}(t) - 1]\alpha x_B(t+\tau_B) \\ &\quad - \tilde{h}_{AB}[\kappa'_{AB}(t_-) - 1]\psi_A(t)\alpha x_B(t_- + \tau_B), \end{aligned} \tag{22}$$

$$\tilde{z}_A(t) = z_A(t) - \psi_A(t)z_A(t_-). \tag{23}$$

$\tilde{\varepsilon}_A(t)$ denotes the residual SI after the DASIC process that is induced by the AFE impairments. Eq. (22) implies that the residual SI $\tilde{\varepsilon}_A(t)$ is zero only if $\theta'_A(t) = \theta'_B(t+\tau_B)$ and $\tau_A = 0$. More specifically, if $\theta'_A(t) = \theta'_B(t+\tau_B)$, $\kappa'_{AB}(t)$ of Eq. (11) is one for any t, resulting in $\tilde{\varepsilon}_A(t) = \varepsilon_A(t)$ from Eq. (22). On the other hand, if $\tau_A = 0$, we derive $\kappa_{AA}(t) = 1$ from Eqs. (10)–(12), resulting in $\varepsilon_A(t) = 0$ from Eq. (18). As the result, we have $\tilde{\varepsilon}_A(t) = 0$.

Figure 3 shows eye diagrams of the DASIC output for MSK and GMSK ($B_G T_s = 0.5$) signaling in an ideal case of $\tau_A = \tau_B = 0$ without AFE impairments. For the visualization, the noise term $z_A(t)$ is zero and $\tilde{h}_{AB}\alpha = 1$. In both cases, the eye apertures are maximized every $2(k+1)T_s$ and $2kT_s$ in the real and imaginary amplitudes, respectively. However, in GMSK, due to the presence of inter-symbol interference (ISI) induced by Gaussian filtering, the aperture is reduced.

Assuming the ideal sampling time at $t = kT_s + \delta$ that maximizes the eye aperture, the ADC of Eq. (19) yields

$$\tilde{y}_A[k] = \tilde{h}_{AB}\alpha\tilde{x}_B[k] + \tilde{\varepsilon}_A[k] + \tilde{z}_A[k], \tag{24}$$

where we have

$$\tilde{x}_B[k] = x_B[k] - \psi_A[k]x_B[k-1], \tag{25}$$

$$\tilde{z}_A[k] = z_A[k] - \psi_A[k]z_A[k-1]. \tag{26}$$

Equation (24) implies that $\tilde{y}_A[k]$ is represented by a simple linear model where $\tilde{x}_B[k]$ is given by the superposed CBB of $x_B[k]$ and $x_B[k-1]$.

The second moments of $\tilde{x}_B[k]$ and $\tilde{z}_A[k]$ are given by $\mathbb{E}\left\{|\tilde{x}_B[k]|^2\right\} = 2\mu$, $(0 \le \mu \le 1)$ and $\mathbb{E}\left\{|\tilde{z}_A[k]|^2\right\} = 2\beta = 2\frac{N_0}{T_s}$, respectively. Figure 4 characterizes equivalent signal density $\mathbb{E}\left\{|\tilde{x}_B[k]|^2\right\} = 2\mu$ at the continuous-time t according to the delay time of the node B τ_B. The value of μ is

[†]If the analog circuitry of the DASIC is difficult to implement from the cost perspective, Fig. 2 can be implemented in the digital domain as an alternative. In this case, the ADC shown in Fig. 1 is placed in front of the DASIC and can operate at the same sampling rate as the symbol rate of the MAP detector.

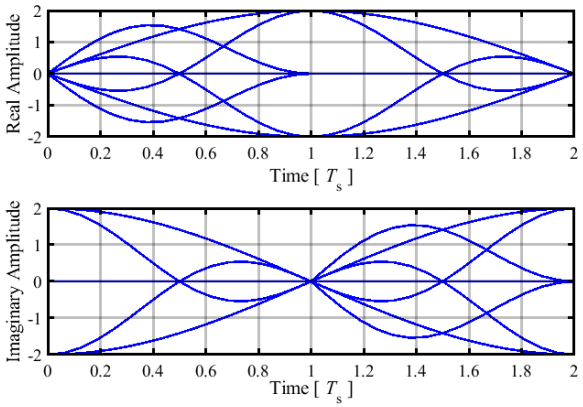

(a) MSK: $B_G T_s = \infty$.

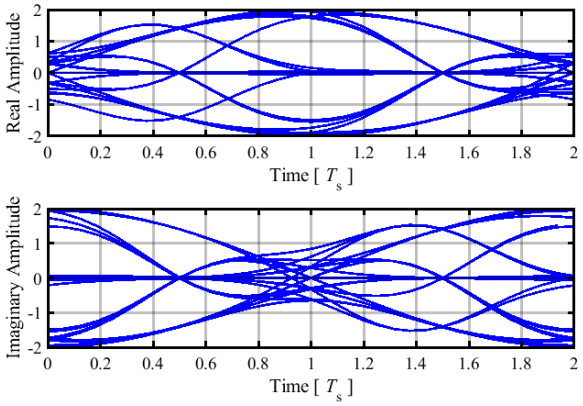

(b) GMSK: $B_G T_s = 0.5$.

Fig. 3 Eye diagrams of the DASIC output $\tilde{y}_A(t)$ for MSK and GMSK: $\eta = 0.5$ where $\tilde{h}_{AB}\alpha = 1$ without AFE impairments.

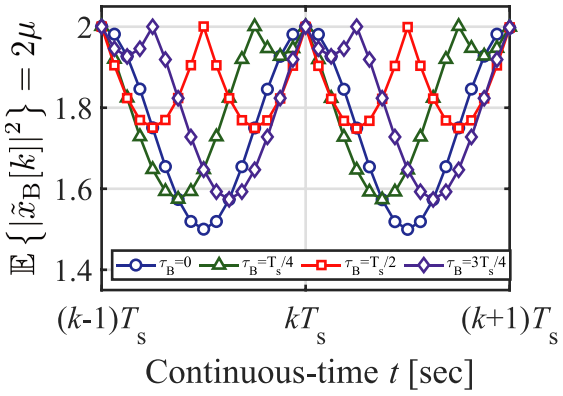

(a) MSK: $B_G T_s = \infty$.

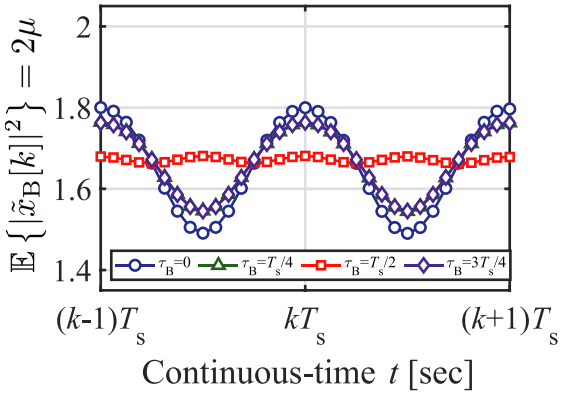

(b) GMSK: $B_G T_s = 0.5$.

Fig. 4 Equivalent signal density $\mathbb{E}\{|\tilde{x}_B[k]|^2\} = 2\mu$ at the continuous time t according to the delay time of the node B τ_B.

maximized at the timing kT_s by adjusting the sample timing δ of ADC. As shown in (a), MSK can keep $\mu = 1$ if δ is appropriate. On the other hand, GMSK with $B_G T_s = 0.5$ in (b) is subject to the energy loss caused by the delay time of the node B τ_B. The maximum loss from the ideal delay time $\tau_B = 0$ is $10\log_{10}\frac{1.80}{1.68} = 0.3$ [dB] at $\tau_B = T_s/2$. Note that the curves of $\tau_B = T_s/4$ and $3T_s/4$ are almost the same because of the phase-circularity. In the case of asynchronous IBFD, structurally, τ_B cannot maintain at zero. However, the maximum loss is only 0.3 [dB]; thus, the negative effect is not significant. From this point forward, we assume $\tau_B = 0$ for ease of discussions in this paper.

The signal-to-interference plus noise power ratio (SINR) of the DASIC output is given by

$$\rho = \frac{\mathbb{E}\left\{\left|\tilde{h}_{AB}\alpha\tilde{x}_B[k]\right|^2\right\}}{\mathbb{E}\left\{|\tilde{\varepsilon}_A[k] + \tilde{z}_A[k]|^2\right\}} = \frac{2\left|\tilde{h}_{AB}\right|^2\alpha^2\mu}{\mathbb{E}\left\{|\tilde{\varepsilon}_A[k]|^2\right\} + 2\beta} = \frac{1}{\frac{\mathbb{E}\{|\tilde{\varepsilon}_A[k]|^2\}}{2|\tilde{h}_{AB}|^2\alpha^2\mu} + \left(\mu|h_{AB}|^2\frac{E_s}{N_0}\right)^{-1}}. \quad (27)$$

To demonstrate the validity of the DASIC, in terms of the interference suppression capability, Fig. 5 exhibits the SINR ρ property of the DASIC output against $\zeta = |h_{AB}|^2/|h_{AA}|^2$ and τ_A. As an example, the instantaneous $|h_{AB}|^2\frac{E_s}{N_0}$ is 10 [dB]. The phase noise at the LOs of the transmitter and receiver is emulated by a model of the phased lock loop (PLL) based CMOS frequency synthesizer with the power spectrum density (PSD). In accordance with the requirements for Bluetooth applications, the PSD is defined as -89 [dBc/Hz] at 500 [kHz] and -121 [dBc/Hz] at 2 [MHz]. The symbol rate $1/T_s$ is 1 [MHz]. In Fig. 5(a), the delay time is $\tau_A \in \{0, 10^{-9}, 10^{-6}\}$ [sec]. In Fig. 5(b), the value of $\zeta = |h_{AB}|^2/|h_{AA}|^2$ is $\{-20, -15, -10\}$ [dB]. As a comparison with the traditional IBFD, the performance of the ASIC is depicted in the figure. In the ASIC, the channel state of $h_{AA}\alpha\xi_A(t+\tau_A)$ is estimated by the least square (LS) criterion with the aid of a 16-bit pilot sequence. Note that the 16-bit pilot sequences of nodes A and B are not orthogonal due to asynchronous IBFD.

Let us focus on Fig. 5(a). In the case of $\tau_A = 0$ [sec], the phase noise behavior can be completely eliminated by the IQ mixer in the receiver of node A. The ASIC suffers from pilot contamination due to asynchronous IBFD, resulting in lower SINR due to residual SI. In the case of $\tau_A = 10^{-9}$ [sec] = 1 [nsec], the SINR is severely degraded if ζ is low. This behavior makes it difficult to implement IBFD. If $\tau_A = 10^{-6}$ [sec] = 1 [μsec], the SINR of the DASIC is worse than that of the ASIC. This is because the differential

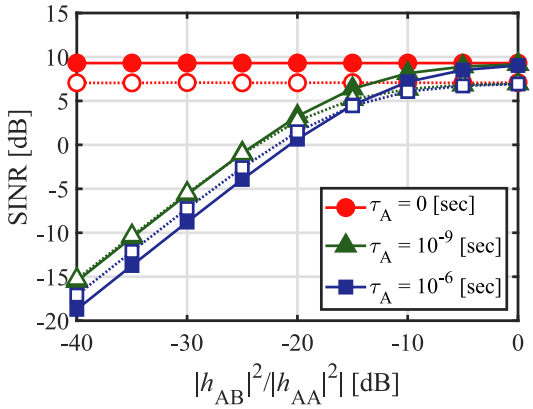

(a) SINR vs. $\zeta = |h_{AB}|^2/|h_{AA}|^2$.

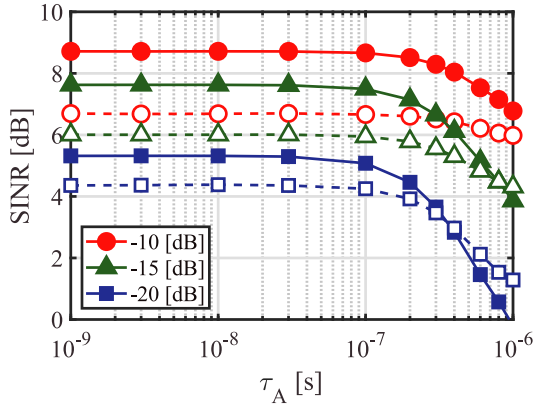

(b) SINR vs. τ_A: The values in the legend indicate $\zeta = |h_{AB}|^2/|h_{AA}|^2$.

Fig. 5 SINR with phase noise impairments: Dashed and solid lines are of the ASIC and DASIC, respectively.

structure is broken. However, because the communication distance is short, the probability that $\tau_A = 1$ [μsec] will occur is low. Next, let us move our focus to Fig. 5(b). The SINR of DASIC is higher than ASIC when τ_A is shorter than 300 [nsec] when $\zeta = |h_{AB}|^2/|h_{AA}|^2 = -20$ [dB] of the lowest target in this paper. The figure emphasizes the importance of phase noise behavior in IBFD considerations.

4. MAP Detector for DASIC Output

As an example, let us consider GFSK signaling with $B_G T_s$, which can be fully captured by a memory size of $L = 3$. Denoting a weight factor as $w_l \triangleq 2\pi\eta q(\Delta t + lT_s)$, $(l \in \{0,1,2\})$ for Gaussian spectrum shaping, the components $x_B[k]$ and $x_B[k-1]$ in the superposed CBB signal $\tilde{x}_B[k]$ of Eq. (25) are expressed as

$$\begin{aligned} x_B[k] = &\exp\{\mathrm{j}(w_0 a_B[k] + w_1 a_B[k-1] \\ &+ w_2 a_B[k-2]) + \mathrm{j}\sigma[k]\}, \end{aligned} \tag{28}$$

$$\begin{aligned} x_B[k-1] = &\exp\{\mathrm{j}(w_0 a_B[k-1] + w_1 a_B[k-2]) \\ &+ \mathrm{j}\sigma[k]\}, \end{aligned} \tag{29}$$

where $\sigma[k]$ denotes a state that is defined by

$$\sigma[k] = \pi\eta \sum_{l'=0}^{k-3} a_B[l']. \tag{30}$$

On the other hand, the phase shift $\psi_A[k]$ in Eq. (25) is given by

$$\begin{aligned} \psi_A[k] = &\exp\{\mathrm{j}w_0(a_A[k] - a_A[k-1]) \\ &+ \mathrm{j}w_1(a_A[k-1] - a_A[k-2]) \\ &+ \mathrm{j}\pi\eta a_A[k-2]\}. \end{aligned} \tag{31}$$

4.1 MSK Signaling

For an intuitive understanding of the structure of the superposed CBB signal, at first, let us consider MSK signaling, i.e., $\eta = 0.5$ and $B_G T_s = \infty$. In this case, the principal values, in terms of the exponential function, of $\sigma[k]$ are one of four states: $\mathcal{U} = \{0, \frac{\pi}{2}, \pi, \frac{3\pi}{2}\}$. When the ADC samples at an appropriate timing Δt that maximizes the eye aperture, the weight factors are $w_0 = 0$ and $w_1 = w_2 = \pi/2$, resulting in

$$x_B[k] = \exp\left\{\mathrm{j}\frac{\pi}{2}(a_B[k-1] + a_B[k-2]) + \mathrm{j}\sigma[k]\right\}, \tag{32}$$

$$x_B[k-1] = \exp\left\{\mathrm{j}\frac{\pi}{2}a_B[k-2] + \mathrm{j}\sigma[k]\right\}, \tag{33}$$

$$\psi_A[k] = \exp\left\{\mathrm{j}\frac{\pi}{2}a_A[k-1]\right\}. \tag{34}$$

Now, denoting $\delta[k] = a_B[k] - a_A[k] \in \{-2, 0, 2\}$, Eq. (25) is rewritten as

$$\begin{aligned} \tilde{x}_B[k] &= \exp\left\{\mathrm{j}\frac{\pi}{2}(a_B[k-1] + a_B[k-2]) + \mathrm{j}\sigma[k]\right\} \\ &\quad - \exp\left\{\mathrm{j}\frac{\pi}{2}(a_B[k-1] + a_B[k-2]) + \mathrm{j}\sigma[k]\right\} \\ &= \mathrm{j}\delta[k-1]\exp\left\{\mathrm{j}\frac{\pi}{2}a_B[k-2] + \mathrm{j}\sigma[k]\right\} \\ &= \begin{cases} 2\exp[\mathrm{j}u_A[k]], & (\delta[k-1] \neq 0) \\ 0, & (\delta[k-1] = 0) \end{cases}, \end{aligned} \tag{35}$$

where we have

$$u_A[k] = \frac{\pi}{2}\left(a_B[k-2] + \frac{\delta[k-1]}{2}\right) + \sigma[k] \in \mathcal{U}. \tag{36}$$

Equation (35) implies that the superposed CBB $\tilde{x}_B[k+1]$ is always zero if node B's information $a_B[k]$ is identical to node A's information $a_A[k]$. Otherwise, $\tilde{x}_B[k+1]$ belongs to one of the states $\mathcal{U}$.

An example of a scatter diagram of the DASIC outputs $\tilde{y}_A[k]$ is depicted in Fig. 6. The Euclidean distance from the DASIC output $\tilde{y}_A[k]$ to each of the five states $\mathcal{X} = \{0, 2\exp[\mathrm{j}\mathcal{U}]\} = \{0, 2, 2\mathrm{j}, -2, -2\mathrm{j}\}$ obeys the complex-valued Gaussian distribution with zero mean and 2β variance. When the occurrences of $a_A[k] = \pm 1$ and $a_B[k] = \pm 1$ are equiprobable, the occurrence probability of $\tilde{x}_B[k]$ is given by

$$\Pr[\tilde{x}_B[k] = 0] = 1/2, \tag{37}$$

$$\Pr[\tilde{x}_B[k] = \{2, 2\mathrm{j}, -2, -2\mathrm{j}\}] = 1/8. \tag{38}$$

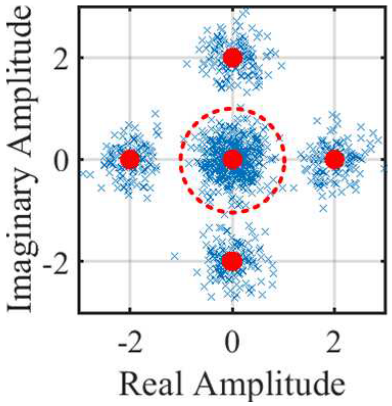

Fig. 6 Scatter plot of the DASIC output $\tilde{y}_A[k]$ where $\tilde{h}_{AB}\alpha = 1$: $\times$ and $\bullet$ indicate the scatter of $\tilde{y}_A[k]$ and $\tilde{x}_B[k] \in \{0, 2, 2j, -2, -2j\}$, respectively.

Therefore, the threshold value for simple hard decision is set to ± 1, which is the stochastic midpoint. According to (35), a criterion for the simple hard decision is formulated as

$$\hat{a}_B[k-1] = \begin{cases} a_A[k-1], & |\tilde{x}_B[k]| < |\tilde{h}_{AB}|\alpha \\ -a_A[k-1], & \text{others} \end{cases}. \quad (39)$$

The bits of nodes A and B are the same ($a_A[k-1] = a_B[k-1]$), $|\tilde{x}_B[k]|$ is inside the circle with radius $|\tilde{h}_{AB}|\alpha$. Otherwise, $|\tilde{x}_B[k]|$ is outside the circle. This method does not request phase information of h_{BA} and the computational complexity is extremely low. However, probabilistic behavior cannot be captured.

For optimal detection in Gaussian channels, the information bit $a_B[k]$ coming from node B to node A is derived by finding the maximum *a-posteriori* probability (MAP) as

$$\hat{a}_B[k] = \arg \max_{a \in \{\pm 1\}} \Pr[a_B[k] = a | \tilde{y}_A[k+1]]. \quad (40)$$

Recalling the relationship discussed in Eq. (35), with the aid of perfect knowledge on the own message $a_A[k]$, the constituent *a-posteriori* probability is obtained by

$$\begin{aligned} &\Pr[a_B[k] = a_A[k] | \tilde{y}_A[k+1]] \\ &\quad = \Pr[\tilde{x}_B[k+1] = 0 | \tilde{y}_A[k+1]], \end{aligned} \quad (41)$$

$$\begin{aligned} &\Pr[a_B[k] = -a_A[k] | \tilde{y}_A[k+1]] \\ &\quad = \Pr[\tilde{x}_B[k+1] \neq 0 | \tilde{y}_A[k+1]], \end{aligned} \quad (42)$$

where

$$\begin{aligned} &\Pr[\tilde{x}_B[k+1] \neq 0 | \tilde{y}_A[k+1]] \\ &= \sum_{x \in \{2,2j,-2,-2j\}} \Pr[\tilde{x}_B[k+1] = x | \tilde{y}_A[k+1]]. \end{aligned} \quad (43)$$

On the basis of Bayes' theorem, the *a-posteriori* probability is rewritten as

$$\begin{aligned} &\Pr[\tilde{x}_B[k] = x | \tilde{y}_A[k]] \\ &\quad = \frac{p(\tilde{y}_A[k] | \tilde{x}_B[k] = x) \Pr[\tilde{x}_B[k] = x]}{p(\tilde{y}_A[k])}, \end{aligned} \quad (44)$$

where $p(\tilde{y}_A[k] | \tilde{x}_B[k] = x)$ is the PDF given by

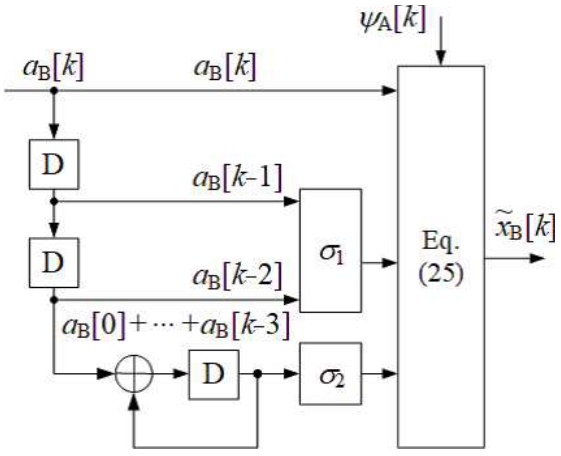

Fig. 7 Structure of IIR filter of signal component $\tilde{x}_B[k]$ included in DASIC output $\tilde{y}_A[k]$.

$$\begin{aligned} &p(\tilde{y}_A[k] | \tilde{x}_B[k] = x) \\ &\quad = \frac{1}{2\pi\beta} \exp\left[-\frac{\left| \tilde{y}_A[k] - \tilde{h}_{AB}\alpha x \right|^2}{2\beta} \right]. \end{aligned} \quad (45)$$

Note that $p(\tilde{y}_A[k])$ is a constant value in terms of the search problem of the maximum value in Eq. (40). Thus, we may replace $p(\tilde{y}_A[k])$ with unity.

4.2 GMSK Signaling

In GMSK signaling, we must pay attention to the fact that we should take into account the infinite impulse response (IIR) filter structure of Eq. (4) to fully capture the amount of mutual information between $\tilde{y}_A[k]$ and $a_B[k]$. Here, let us investigate the MAP detector for the IIR-filtered signal, which can achieve optimal performance in terms of probabilistic theory. According to the MAP framework, the *a-posteriori* LLR is defined by

$$\lambda_B[k] = \ln \frac{\Pr[a_B[k] = +1 | \{\tilde{y}_A[k]\}]}{\Pr[a_B[k] = -1 | \{\tilde{y}_A[k]\}]}, \quad (46)$$

where $\{\tilde{y}_A[k]\}$ indicates a sequence of $\tilde{y}_A[k]$. To compute the LLR $\lambda_B[k]$ with reasonable computational efforts, we focus on the IIR filter structure of Eq. (4).

Figure 7 illustrates the filter structure using memory size $L = 3$ as an example. On the basis of the trellis diagram depicted from Fig. 7, the LLR can be obtained by the Bahl–Cocke–Jelinek–Raviv (BCJR) algorithm [28] without requiring a large computational burden†. Assuming BCJR is applied for GFSK demodulation in both ASIC and DASIC, the complexity relies on the number of states in the BCJR

†Although this paper assumes the identical GFSK modulation in nodes A and B, the same DASIC technique can be used for SI cancellation when changing to other modulation schemes. However, note that changes in the combination of modulation schemes complicate the trellis structure, which causes changes in the error correction effect in the MAP signal detector, as well as in the iterative gain for the IDD regime.

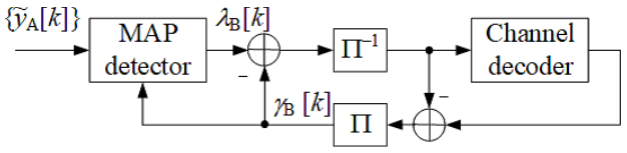

Fig. 8 Schematic of the IDD receiver.

algorithm. In this paper, $L = 3$ is used for $B_G T_s = 0.5$ pulse shaping of both ASIC and DASIC. If $B_G T_s$ is smaller than 0.5, the L should be a larger value than 3, resulting in a large number of states. In this paper, the number of states is negligibly small, i.e., $4^{L-1} = 16$ states. It is equivalent to binary convolutional code with constraint length 4. Thus, the complexity is not so high.

Here, one element of the Cartesian product set (four states) of $a_B[k-1] = \{\pm 1\}$ and $a_B[k-2] = \{\pm 1\}$ is represented by σ_1. In addition, one element of the four-state set $\mathcal{U}$ is represented by σ_2. From these states σ_1 and σ_2 as well as the DASIC input $a_B[k]$, the superposed CBB signal $\tilde{x}_B[k]$ can be reproduced, and the input/output relationship is denoted by $\tilde{x}_B[k] = f(a_B[k], \sigma_1, \sigma_2)$. The transition (joint) probability required in the BCJR process is given by

$$\begin{aligned}&\Pr\left[a_B[k] = \{\pm 1\}, \sigma_1, \sigma_2 | \tilde{y}_A[k]\right] \\ &\propto \exp\left\{-\frac{\left|\tilde{y}_A[k] - \tilde{h}_{AB}\alpha f(a_B[k], \sigma_1, \sigma_2)\right|^2}{2\beta}\right\} \\ &\quad \cdot \exp\left\{a_B[k]\frac{\gamma_B[k]}{2}\right\}, \end{aligned} \tag{47}$$

where $\gamma_B[k]$ is the *a-priori* LLR, which represents the confidence in the prior knowledge of $a_B[k]$, and it is defined by

$$\gamma_B[k] = \ln \frac{\Pr[a_B[k] = +1]}{\Pr[a_B[k] = -1]}. \tag{48}$$

Note that $\gamma_B[k]$ is zero if there is no prior information.

4.3 IDD Receiver

If ECC and an interleaver (Π) are used at the transmitter side, it is possible to perform IDD, in which signal detection is achieved by exchanging extrinsic LLRs between the MAP detector and the error correction decoder [31].

Figure 8 shows the schematic of the IDD receiver. With the aid of the *a-priori* LLR $\gamma_B[k]$, Eq. (46) calculates the *a-posteriori* LLR $\lambda_B[k]$. Subsequently, the extrinsic LLR is obtained by subtracting the *a-priori* LLR $\gamma_B[k]$ from the *a-posteriori* LLR $\lambda_B[k]$. The resulting extrinsic LLR is deinterleaved (Π^{-1}) and applied to the channel decoder. The extrinsic LLR is updated at the channel decoder after the error correction process. The updated LLR is fed back to the MAP detector via the interleaver as the *a-priori* LLR $\gamma_B[k]$. After repeating these LLR exchanges, the decision value of the information bit is obtained from the channel decoder.

Note that the computational complexity of the iteration process linearly increases according to the allowed number of iterations. Thus, the number of states in BCJR is a dominating factor in terms of the complexity of ASIC and DASIC.

Table 1 Simulation parameters.

Modulation	GMSK ($\eta = 0.5$, $B_G T_s = 0.5$, $L = 3$)
Detector	Log-MAP (Jacobian-log)
Packet length	1024 symbols
Channel encoder	None, Convolutional code
Coding rate	1, 1/2 (Constraint length = 4)
Decoder	None, Log-MAP (Jacobian-log)
Num. of iterations	1, 16
Interleaver	Random
Channel model	AWGN + Rayleigh fading

4.4 Channel Estimations

To carry out the MAP detection of Eqs. (40) and (46), the values h_{AB} and β are estimated from the preamble. Now, we assume that an M-bit pilot sequence is appended in front of the data sequence. Based on the LS criterion, the estimated values can be obtained by

$$\hat{h}_{AB} = \frac{\sum_{k=1}^{M} \tilde{y}_A[k]\tilde{x}_B[k]^*}{\alpha \sum_{k=1}^{M} |\tilde{x}_B[k]|^2}, \tag{49}$$

$$\hat{\beta} = \frac{1}{M}\sum_{k=1}^{M} \frac{|\tilde{y}_A[k]|^2}{\alpha^2} - \left|\hat{h}_{AB}\right|^2. \tag{50}$$

As shown in Eq. (24), the signal model after SI cancellation is characterized by the single-input single-output (SISO) aditive white Gaussian noise (AWGN) model, assuming that random components $\tilde{\varepsilon}_A[k] + \tilde{z}_A[k]$ obey Gaussian distribution. In this simple signal model, the typical channel estimation is LS estimation. If long-term statistics of the channel state $\mathbb{E}\{|h_{AB}|^2\}$ are available, MAP estimation with high accuracy is feasible even in the channel estimation, but such long-term statistics are not available because we assume random access in the IoT scenario. Iterative channel estimation is a promising technique for IDD structures. However, owing to space limitations in this paper, we do not evaluate the effect of iterative channel estimation in simulations.

5. Numerical Results

Computer simulations were conducted to verify the effectiveness of the proposed DASIC. The simulation conditions are summarized in Table 1. The modulation scheme is GMSK ($\eta = 0.5$, $B_G T_s = 0.5$, $L = 3$), and the MAP algorithm based on the Jacobian logarithm is used for its demodulation. At this time, to cope with the tail bit problem of the MAP demodulator, dummy bits of $L - 1$ length are appended after the information data block. In the non-coded scenario without ECC, any channel code is not applied, resulting in 1024 data bits in one packet with 1024 symbols. On the other hand, in the coded scenario with the aid of ECC, half-rate non-systematic convolutional (NSC) code with Generator polynomials $G_0(x) = 1 + x + x^2 + x^3$ and $G_1(x) = 1 + x^2 + x^3$ is utilized. The code length is 1024 coded bits, i.e., the

information length is 509 bits and the tail length for state termination of the convolutional code is 3 bits. Its decoding employs the MAP algorithm. In the case of IDD, the number of iterations for LLR exchange between the MAP detector and the channel decoder is 16. At this time, we used a random permutation in the interleaver. The channel model assumes the AWGN channel is affected by flat Rayleigh fading. IQ imbalance is assumed to be negligibly small in this paper.

As a comparison with the traditional IBFD, i.e., a baseline scheme, the performance of the ASIC with the aid of CSI is evaluated. $L = 3$ is used for both ASIC and DASIC. Thus, the dominating complexity order of BCJR is the same. When IDD is applied in DASIC, the complexity linearly increases according to the allowed number of iterations.

5.1 Without Phase Noise Impairments

Figure 9 shows the PER characteristics of the DASIC without phase noise impairments for $|h_{\mathrm{AB}}|^2 E_{\mathrm{s}}/N_0$. Although the channel obeys Rayleigh fading, the horizontal axis is the instantaneous $|h_{\mathrm{AB}}|^2 E_{\mathrm{s}}/N_0$, not the average. As a result, it is equivalent to the channel affected by phase rotation without amplitude fluctuations.

Figure 9(a) presents the detection capability when the channel states and noise variance are ideally estimated. Thus, $\tilde{h}_{\mathrm{AB}}$ and β are perfectly known at node A in the DASIC. On the other hand, h_{AA}, h_{AB}, and N_0 are perfectly captured in the ASIC. Three types of PER are evaluated for each DASIC and ASIC. The first and second types are without and with the channel encoder ("w/o ECC," "w/ ECC"). The last type of PER is IDD with the aid of LLR exchange between the MAP detector and the decoder. As can be seen in the figure, the ASIC achieves a gain of approximately 2 [dB] compared to the DASIC for all types of PER. However, this comparison is unfair because the ASIC can completely eliminate SI in this case. It is obvious that the DASIC is not useful in the ideal scenario.

Now, let us shift the focus to Figs. 9(b) and (c), which show the PER when the channel and noise variance are estimated by 32- and 16-bit pilot sequences, respectively. Due to the pilot contamination induced by asynchronous IBFD between nodes A and B, a longer pilot is necessary for the ASIC to suppress channel estimation errors enhanced by the non-orthogonal pilot sequences. Figure 9(b) shows the impairments caused by the pilot contamination. Even if the 32-bit pilot is available, the slope of the PER curves of the ASIC is low. As a result, DASIC outperforms ASIC at the

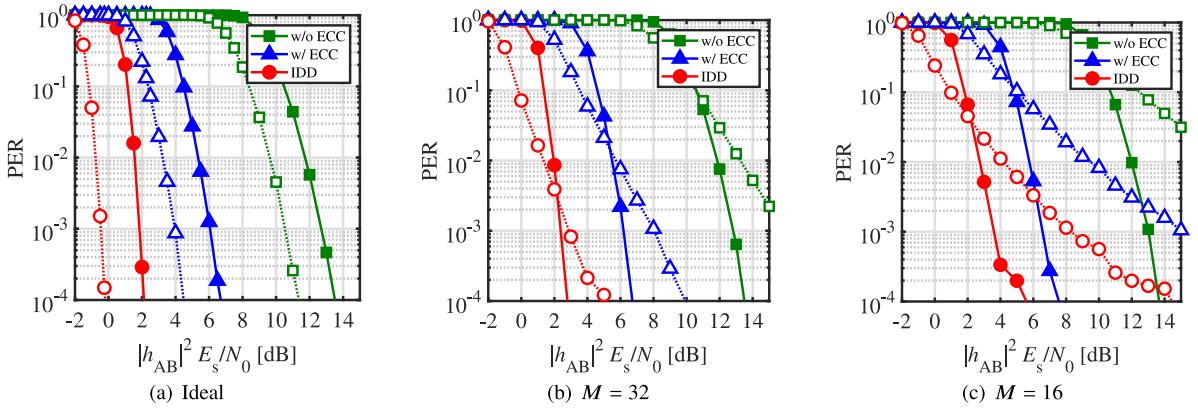

Fig. 9 PER performance without phase noise impairments ($\zeta = -20$ [dB]): dashed and solid lines are of the ASIC and DASIC, respectively.

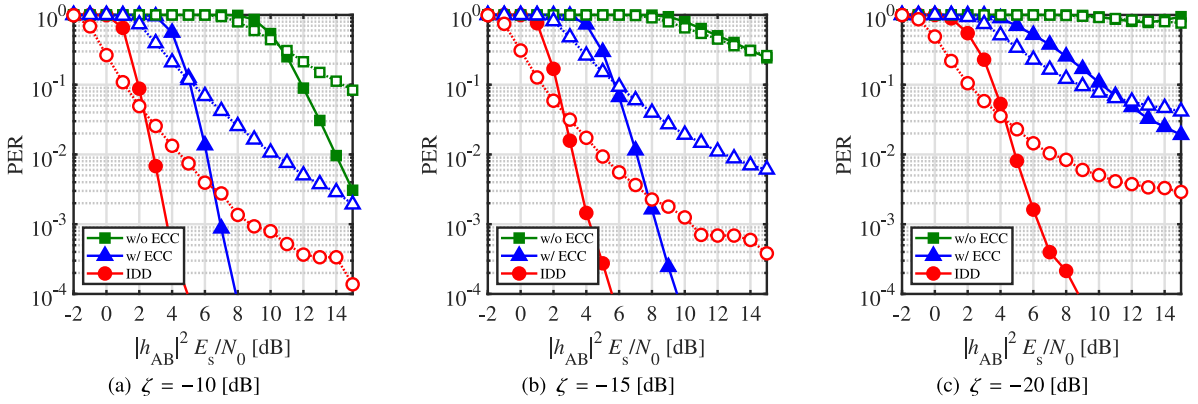

Fig. 10 PER performance with phase noise impairments ($\tau_{\mathrm{A}} = 1$ [nsec], $M = 16$): dashed and solid lines are of the ASIC and DASIC, respectively.

lower PER target. Furthermore, when the pilot length is shorter, such as $M = 16$, as shown in Fig. 9(c), we can see that the DASIC has large advantages. The results explicitly demonstrate that the proposed DASIC algorithm is effective for the pilot contamination problem in asynchronous IBFD.

5.2 With Phase Noise Impairments

As discussed in Fig. 5, IBFD seriously suffers from the negative effects of phase noise. Figure 10 visualizes the negative effects of phase noise impairments for the delay $\tau_A = 1$ [nsec] and 16-bit pilot sequence ($M = 16$). In the case of $\zeta = -10$ [dB] of Fig. 10(a), the performance of the ASIC and DASIC-"w/o ECC" is degraded compared to that in Fig. 9(c). However, "w/ ECC" and "IDD" of the DASIC achieve almost the same performance. In the case of $\zeta = -15$ [dB], it is subject to 1 [dB] penalty at PER = 10^{-3} in the DASIC "w/ ECC." Finally, in the case of $\zeta = -20$ [dB], it is subject to 2 [dB] penalty at PER = 10^{-3} even in "IDD." However, there is no PER error floor in the curve. Furthermore, in the other simulation, we have confirmed the PER = 0.1 is achieved by the DASIC-"IDD" at $|h_{AB}|^2 E_s/N_0 = 8$ [dB] in the case of $\zeta = -25$ [dB] in the other simulations. These results explicitly validate the proposed DASIC-IDD algorithm even in the presence of phase noise when SIR is lager than $\zeta = -20$ [dB], despite the fact that the ASIC is more sensitive to phase noise behavior. The most impressive feature of the DASIC is the fact that asynchronous IBFD is realized.

When the SIR is below $\zeta = -20$ [dB], the proposed scheme is not so effective in the presence of phase noise effects because it leads to a significant increase in the transmission power to meet the required PER. Unfortunately, it is difficult to realize IBFD using the proposed method alone, which needs to support typical SIRs of −90 to −70 [dB] in short-range communications for wireless IoT. It is assumed that the proposed method will be used in combination with conventional self-interference cancellation techniques with a total of approximately 60 [dB] interference reduction: approximately 20 [dB] attenuation with antenna isolation, and approximately 40 [dB] with the other passive analog canceller. However, the scale of analog circuits required to achieve significant interference suppression with a passive analog canceller is large, making them unsuitable for wireless IoT applications. To address this problem, it is necessary to consider implementing the proposed method with a technique to suppress the effects of phase noise.

6. Conclusion

In this paper, we proposed a novel DASIC algorithm for asynchronous IBFD GFSK, which is designed for wireless IoT. The DASIC incorporates the principle of the differential codec. Because of the differential structure, the DASIC can suppress SI without the CSI estimation of SI. To improve the detection capability, IDD for the DASIC was appropriately investigated.

In ideal channel estimation conditions, the DASIC has the disadvantage of decreasing the reception sensitivity compared to the ASIC. However, when the CSI contains estimation errors induced by pilot contamination, the detection capability of the DASIC is better than that of the ASIC. Furthermore, with the aid of IDD, the SIR tolerance is improved to approximately 20 [dB] for maintaining PER = 10^{-3}. Although the utilization field is limited to indoor environments, the results explicitly demonstrate the possibility of the realization of asynchronous IBFD in combination with conventional antenna isolation and analog SI cancellation techniques. The asynchronous blind SI cancellation will open new vistas in the utilization of IBFD in wireless IoT. As a future work, practical implementation of analog DASIC circuit is an attractive issue.

Acknowledgments

A part of this work was financially supported by JSPS KAKENHI Grant Number JP21H01332 and grants-in-aid from the Haris Science Research Institute of Doshisha University.

References

[1] K. Chang, "Bluetooth: A viable solution for IoT?," IEEE Wireless Commun., vol.21, no.6, pp.6–7, Dec. 2014.
[2] M.R. Palattella, M. Dohler, A. Grieco, G. Rizzo, J. Torsner, T. Engel, and L. Ladid, "Internet of Things in the 5G era: Enablers, architecture, and business models," IEEE J. Sel. Areas Commun., vol.34, no.3, pp.510–527, March 2016.
[3] K. Hirade, M. Ishizuka, F. Adachi, and K. Ohtani, "Error-rate performance of digital FM with differential detection in land mobile radio channels," IEEE Trans. Veh. Technol., vol.28, no.3, pp.204–212, Aug. 1979.
[4] B.E. Rimoldi, "A decomposition approach to CPM," IEEE Trans. Inf. Theory, vol.34, no.2, pp.260–270, March 1988.
[5] D. Bharadia, E. McMilin, and S. Katti, "Full duplex radios," Proc. ACM SIGCOMM 2013, pp.375–386, Aug. 2013.
[6] Z. Zhang, K. Long, A.V. Vasilakos, and L. Hanzo, "Full-duplex wireless communications: Challenges, solutions, and future research directions," Proc. IEEE, vol.104, no.7, pp.1369–1409, July 2016.
[7] K.E. Kolodziej, B.T. Perry, and J.S. Herd, "In-band full-duplex technology: Techniques and systems survey," IEEE Trans. Microw. Theory Techn., vol.67, no.7, pp.3025–3041, July 2019.
[8] A. Gupta and R.K. Jha, "A survey of 5G network: Architecture and emerging technologies," IEEE Access, vol.3, pp.1206–1232, 2015.
[9] Z. Zhang, X. Chai, K. Long, A.V. Vasilakos, and L. Hanzo, "Full duplex techniques for 5G networks: Self-interference cancellation, protocol design, and relay selection," IEEE Commun. Mag., vol.53, no.5, pp.128–137, May 2015.
[10] V. Wong, Key Technologies for 5G Wireless Systems, Cambridge University Press, 2017.
[11] M. Duarte, C. Dick, and A. Sabharwal, "Experiment-driven characterization of full-duplex wireless systems," IEEE Trans. Wireless Commun., vol.11, no.12, pp.4296–4307, Dec. 2012.
[12] A. Sahai, G. Patel, C. Dick, and A. Sabharwal, "On the impact of phase noise on active cancelation in wireless full-duplex," IEEE Trans. Veh. Technol., vol.62, no.9, pp.4494–4510, Nov. 2013.
[13] E. Everett, A. Sahai, and A. Sabharwal, "Passive self-interference suppression for full-duplex infrastructure nodes," IEEE Trans. Wireless Commun., vol.13, no.2, pp.680–694, Feb. 2014.
[14] B.P. Day, A.R. Margetts, D.W. Bliss, and P. Schniter, "Full-duplex MIMO relaying: Achievable rates under limited dynamic range," IEEE J. Sel. Areas Commun., vol.30, no.8, pp.1541–1553, Sept.

2012.
[15] P. Popovski and H. Yomo, "Physical network coding in two-way wireless relay channels," Proc. IEEE ICC 2007, pp.707–712, June 2007.
[16] Z. Zhang, Z. Ma, Z. Ding, M. Xiao, and G.K. Karagiannidis, "Full-duplex two-way and one-way relaying: Average rate, outage probability, and tradeoffs," IEEE Trans. Wireless Commun., vol.15, no.6, pp.3920–3933, June 2016.
[17] Y. Choi and H. Shirani-Mehr, "Simultaneous transmission and reception: Algorithm, design and system level performance," IEEE Trans. Wireless Commun., vol.12, no.12, pp.5992–6010, Dec. 2013.
[18] D. Korpi, T. Riihonen, V. Syrjälä, L. Anttila, M. Valkama, and R. Wichman, "Full-duplex transceiver system calculations: Analysis of ADC and linearity challenges," IEEE Trans. Wireless Commun., vol.13, no.7, pp.3821–3836, July 2014.
[19] A. Tang and X. Wang, "A-duplex: Medium access control for efficient coexistence between full-duplex and half-duplex communications," IEEE Trans. Wireless Commun., vol.14, no.10, pp.5871–5885, Oct. 2015.
[20] A. Sabharwal, P. Schniter, D. Guo, D.W. Bliss, S. Rangarajan, and R. Wichman, "In-band full-duplex wireless: Challenges and opportunities," IEEE J. Sel. Areas Commun., vol.32, no.9, pp.1637–1652, Sept. 2014.
[21] D. Kim, H. Lee, and D. Hong, "A survey of in-band full-duplex transmission: From the perspective of PHY and MAC layers," IEEE Commun. Surveys Tuts., vol.17, no.4, pp.2017–2046, Fourth quarter 2015.
[22] M. Kobayashi, R. Murakami, K. Kizaki, S. Saruwatari, and T. Watanabe, "Wireless full-duplex medium access control for enhancing energy efficiency," IEEE Trans. Green Commun. Networking, vol.2, no.1, pp.205–221, March 2018.
[23] K. Komatsu, Y. Miyaji, and H. Uehara, "Basis function selection of frequency-domain Hammerstein self-interference canceller for in-band full-duplex wireless communications," IEEE Trans. Wireless Commun., vol.17, no.6, pp.3768–3780, June 2018.
[24] G. Qiao, S. Gan, S. Liu, L. Ma, and Z. Sun, "Digital self-interference cancellation for asynchronous in-band full-duplex underwater acoustic communication," Sensors, vol.18, no.6, 1700, May 2018.
[25] J. Choi, D. Kim, S. Lee, H. Lee, J. Bang, and D. Hong, "A new frame structure for asynchronous in-band full-duplex systems," Proc. IEEE PIMRC 2015, pp.487–491, 2015.
[26] A. Munari, P. Mähönen, and M. Petrova, "A stochastic geometry approach to asynchronous aloha full-duplex networks," IEEE/ACM Trans. Netw., vol.25, no.6, pp.3695–3708, 2017.
[27] V. Towhidlou and M. Shikh-Bahaei, "Adaptive full-duplex communications in cognitive radio networks," IEEE Trans. Veh. Technol., vol.67, no.9, pp.8386–8395, 2018.
[28] L. Hanzo, T. Liew, and B. Yeap, Turbo Coding, Turbo Equalisation and Space-Time Coding, Wiley, New York, 2002.
[29] D. MacKay, Information Theory, Inference and Learning Algorithms, Cambridge University Press, 2003.
[30] J. Hagenauer, E. Offer, and L. Papke, "Iterative decoding of binary block and convolutional codes," IEEE Trans. Inf. Theory, vol.42, no.2, pp.429–445, March 1996.
[31] M. Tuchler and A.C. Singer, "Turbo equalization: An overview," IEEE Trans. Inf. Theory, vol.57, no.2, pp.920–952, Feb. 2011.
[32] S. Ibi, T. Matsumoto, R. Thoma, S. Sampei, and N. Morinaga, "EXIT chart-aided adaptive coding for multilevel BICM with turbo equalization in frequency-selective MIMO channels," IEEE Trans. Veh. Technol., vol.56, no.6, pp.3757–3769, Nov. 2007.
[33] T. Takahashi, S. Ibi, and S. Sampei, "Design of adaptively scaled belief in multi-dimensional signal detection for higher-order modulation," IEEE Trans. Commun., vol.67, no.3, pp.1986–2001, March 2019.
[34] M. Elsayed, A.A.A. El-Banna, O.A. Dobre, W. Shiu, and P. Wang, "Low complexity neural network structures for self-interference cancellation in full-duplex radio," IEEE Commun. Lett., vol.25, no.1, pp.181–185, 2021.
[35] Z. Wang, M. Ma, and F. Qin, "Neural-network-based nonlinear self-interference cancelation scheme for mobile stations with dual-connectivity," IEEE Access, vol.9, pp.53566–53575, 2021.
[36] A. Balatsoukas-Stimming and C. Studer, "Deep unfolding for communications systems: A survey and some new directions," Proc. IEEE SiPS 2019, pp.266–271, 2019.
[37] D. Shirase, T. Takahashi, S. Ibi, K. Muraoka, N. Ishii, and S. Sampei, "Deep unfolding-aided gaussian belief propagation for correlated large mimo detection," Proc. GLOBECOM 2020, pp.1–6, 2020.
[38] J.B. Anderson, T. Aulin, and C.E. Sundberg, Digital Phase Modulation, 1st ed., Springer Publishing Company, 2013.

Shinsuke Ibi received the B.E. degree in advanced engineering from Suzuka College of Technology, Japan, in 2002, and the ME and Ph.D. degrees in communication engineering from Osaka University, Japan, in 2004 and 2006, respectively. From 2005 to 2006, he was a visiting researcher at the Centre for Wireless Communications, University of Oulu, Finland. In 2006, he joined the Graduate School of Engineering, Osaka University. From 2010 to 2011, he was a visiting researcher at the University of Southampton, United Kingdom. In 2019, he moved to Doshisha University, and he is currently a professor in the Faculty of Science and Engineering. His research interests include EXIT-based coding theory, iterative detection, digital signal processing, cognitive radio, and communication theory. He received the 64th, 71th, and 80th Best Paper Awards from IEICE, 2017, 2018, 2019, and 2023 Best Paper Awards from IEICE Communication Society, and the 24th Telecom System Technology Award from the Telecommunication Advancement Foundation. He is a senior member of IEEE.

Takumi Takahashi received his B.E., M.E., and Ph.D. degrees in communication engineering from Osaka University, Osaka, Japan, in 2016, 2017, and 2019, respectively. From 2018 to 2019, he was a visiting researcher at the Centre for Wireless Communications, University of Oulu, Finland. In 2019, he joined the Graduate School of Engineering, Osaka University as an assistant professor. His research interests include belief propagation, compressed sensing, signal processing, and wireless communications. He is a member of IEEE.

Hisato Iwai received the B.E., M.E., and Ph.D. degrees from Kyoto University, Kyoto, Japan in 1987, 1989, and 2001, respectively. In 1989, he joined KDD R&D Laboratories, where he was engaged in research on antennas and propagation in radio communication systems. From 1996 to 1997, he was a visiting scholar at University of California, San Diego (UCSD). Also, he was with Telcordia Technologies NJ as a visiting researcher from 1999 to 2001. From 2004 to 2005, he was a research head at ATR Adaptive Communication Research Laboratories. He is currently a professor at Doshisha University, Kyoto, Japan. His current research interests include propagation models in various radio communication systems, radio transmission systems, applied radio systems, and so on. He is a member of IEEE.